The Utility of GNSS for Earthquake Early Warning in Regions with Sparse Seismic Networks

by Ronni Grapenthin, Michael West, and Jeffrey Freymueller

Abstract   Real-time Global Navigation Satellite Systems (GNSS) data are on their way to being well integrated into earthquake early warning (EEW) systems. The strength of GNSS data lies in the resolution of large dynamic and static displacements. Because of the limits in precision, GNSS data alone cannot resolve small ground displacements due to, for instance, P waves. Therefore, their use is currently limited to refining early warnings with more precise earthquake characteristics, such as magnitudes or ground-motion predictions.

Here, we analyze 1-Hz Global Positioning System (GPS) data from the 24 January 2016 M_w 7.1 Iniskin earthquake, which ruptured 125 km under Cook Inlet in Alaska, to motivate the inclusion of GNSS-derived S-wave measurements into the trigger algorithms of EEW systems in regions lacking dense early-warning instrumentation networks. We derive a relationship between earthquake depth and distance to help determine whether GNSS S-wave observations could expedite warnings to specific locations.

Because the Iniskin earthquake was deep, by the time the S wave reached the surface, the P wave had already been observed over a wide region, limiting the potential for unique contributions from GNSS data to this event. For the same earthquake occurring near the surface, however, S waves derived from GNSS data have the potential to increase the warning time. Regardless of the depth, the Iniskin earthquake is an excellent example of the utility of GNSS in rapidly assessing the magnitude, improving predictions of ground shaking, and estimating the area of impact for the earthquake.

Introduction

After the 2011 M_w 9.0 Tohoku-oki earthquake in Japan (Simons *et al.*, 2011), the utility of real-time Global Navigation Satellite Systems (GNSS, of which the Global Positioning System [GPS] is one constellation) in earthquake early warning (EEW; Allen and Kanamori, 2003) was quickly and widely recognized and implemented. Although the Japanese EEW system detected the earthquake and alarmed the population before strong ground motion reached the shore, the system saturated 117 s after rupture initiation at magnitude M_w 8.1 (Hoshiba *et al.*, 2011). This is explained by the limited frequency band used for magnitude estimates, by the clipping/tilting of some seismic sensors, and, for very long ruptures, by a point-source approximation used in modeling the data may not hold for fitting near-field data or for predicting ground motions. Although real-time GNSS, compared with seismometers, is relatively insensitive to ground motions induced by earthquakes below $M_w \sim 6.0$, particularly to the small coseismic offsets (e.g., Grapenthin *et al.*, 2014a), the technology is capable of measuring very large ground motions and permanent displacements precisely. A number of studies have since demonstrated that high-rate GNSS-based analysis can determine the magnitude of large earthquakes once the rupture finishes and static displacements manifest at observation sites (e.g., Wright *et al.*, 2012; Colombelli *et al.*, 2013; Melgar *et al.*, 2013). Fang *et al.* (2014) demonstrated that the empirical displacement–magnitude relationship of Gutenberg (1945) holds nearly to M_w 9.0 (Tohoku), using Gutenberg's original coefficients. All of these studies demonstrate that rapid magnitude determination is possible using either dynamic or static displacements from GNSS sites (or both).

The ShakeAlert EEW demonstration system for the U.S. West Coast (e.g., Given *et al.*, 2014) has been in development since 2007. Efforts to integrate real-time GNSS analysis and modeling into ShakeAlert and similar systems in other countries resulted in the development of a number of geodetic algorithms, for example, BEFORES (Minson *et al.*, 2014), G-larmS (Grapenthin *et al.*, 2014b), G-FAST (Crowell *et al.*, 2016), and REGARD (Kawamoto *et al.*, 2016) that all take slightly different approaches in determining the size

of an earthquake. Although these algorithms currently operate only in demonstration or development modes, the 2014 M_w 6.0 Napa earthquake (Brocher *et al.*, 2015) demonstrated meaningful contributions from GNSS. G-larmS analyzed the earthquake in real time (Grapenthin *et al.*, 2014a), providing an initial magnitude estimate 24 s after the origin time (OT) as the *S* waves traversed the network. Retrospective analysis showed that, with code optimizations, this time could have been as low as 14 s (8 s *S*-wave travel time, 6 s system latency).

The geodetic algorithms in the ShakeAlert system are triggered by seismic *P*-wave detection, reflecting the common assumption that GNSS has little to contribute to the initial early warning of earthquakes and serves mostly as a rapid response tool to assess strong shaking and source finiteness. The subtle difference between early detection and rapid response is the difference between *P*- and *S*-wave arrival times. Rapid *P*-wave detection is the canonical approach to improve warning times and minimize the shadow zone—the region that will not receive a warning before the shaking arrives. This approach assumes a need for rapid warning in the immediate vicinity of the epicenter, as well as a concern for relatively moderate earthquakes.

This paradigm does not apply in all locations. GNSS may play a more important role for large earthquakes occurring some distance from cities and critical facilities and for earthquakes occurring in areas with sparse instrumentation networks. Although fast warning times remain the goal, in both the distant and sparse scenarios, large *S*-wave displacements may be propagating across geophysical networks many seconds before sufficient observations have been acquired to issue a warning. Because the impact area may be vast for magnitude 8 and 9 earthquakes, rapid detection is of questionable value if not accompanied by an accurate magnitude assessment. If the region has high rates of background seismicity, poor magnitude assessment will inevitably lead to significant false alarms.

The combination of large earthquakes, widely distributed population centers, and relatively sparse instrumentation networks is, in fact, the norm in most of the high-seismic-hazard regions that ring the Pacific, including Alaska, Kamchatka, much of the South American coast, Southeast Asia, and Oceania. In many of these regions, an emphasis on minimizing shadow zones or delivering single-digit warning times may be of less importance than rapidly estimating the magnitude, depth, and full region of impact for an earthquake that could take a minute or more to rupture.

It is important to note that the existing networks of GNSS and seismic sensors are generally neither co-located nor designed for EEW purposes. These independent installations are rooted in the science and monitoring that they support. However, the existing networks are likely to contribute to a single EEW system, because station upgrades are less costly than new installations, and sparse seismic networks, such as in the places mentioned above, may benefit from geodetic triggering.

Here, we use 1-Hz GPS data for the 2016 M_w 7.1 Iniskin earthquake in Alaska to demonstrate the value of *S*-wave phase arrivals derived from GNSS data. We use standard phase detection techniques to demonstrate that accurate *S*-wave observations can be made rapidly enough to be included in EEW triggering algorithms. We apply peak ground displacement scaling relationships (e.g., Fang *et al.*, 2014; Melgar *et al.*, 2015) to determine the magnitude evolution of the event as it may have been inferred during real-time GNSS analysis. Furthermore, we derive a relationship between earthquake depth and epicentral distance to help determine in what situations GNSS *S*-wave triggers might be useful in providing EEWs.

The 2016 M_w 7.1 Iniskin, Alaska, Earthquake

On 24 January 2016, the M_w 7.1 Iniskin earthquake rupture initiated at 125 km depth below the Cook Inlet region of Alaska (Fig. 1). Anchorage (the largest city in Alaska, with a metropolitan population of about 400,000) is 260 km to the northeast from the epicenter. Several modestly sized population centers closer to the epicenter are located on the Kenai Peninsula on the east side of Cook Inlet, including Kenai, Homer, and Seward.

The earthquake occurred within the Pacific plate as a result of down-dip extension in the subducting slab. Though the lower Cook Inlet region has long been recognized as a source of vigorous intermediate-depth slab seismicity, the Iniskin earthquake was one of the largest of its kind to date. The U.S. Geological Survey (USGS) finite-fault model (see Data and Resources) suggests a 60° striking and 66° dipping plane, with a maximum slip of about 3 m between 5 and 10 s after the OT and between 10 and 20 km above the hypocenter.

Peak ground accelerations of 20%–40% *g* corroborate the strong perceived shaking and the related damage (see Data and Resources). USGS "Did You Feel It?" reports (Worden *et al.*, 2012) indicate perceived shaking intensities of VII up to 200 km from the epicenter. Soil compaction, slumping, and liquefaction were damage multipliers, leading to local effects that far exceeded the shaking from the earthquake itself. Fires due to gas leaks in Kenai destroyed several homes and required evacuations. Power outages affected more than 10,000 homes. Although no casualties were reported, these incidents might have been prevented by automated infrastructure regulating systems that are activated by an EEW notification.

Seismic Network and Observations

The broadband seismic network in the vicinity of the earthquake is well distributed, though not dense (Fig. 1). Outside of the Anchorage urban area and some volcano clusters, the spacing of broadband and strong-motion instrumentation is typically many tens of kilometers. Newly installed USArray stations northwest of the earthquake enhanced the coverage significantly. However, broadband stations within
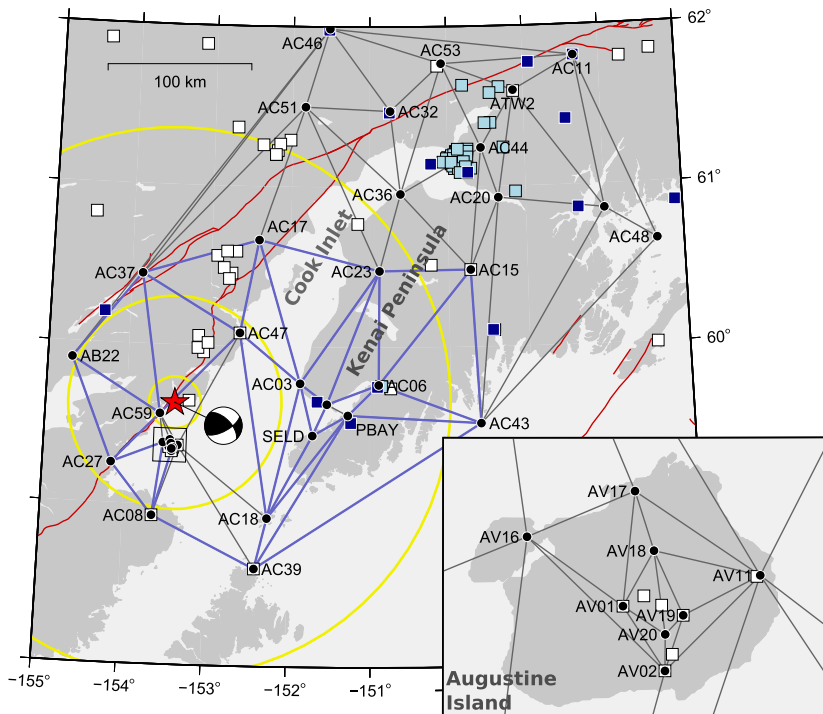
Figure 1. Global Positioning System (GPS) (circles) and seismic (squares) networks in Cook Inlet, Alaska (star marks epicenter). Black circles are continuous high-rate GPS stations; lines connecting them indicate base-station–rover pairs that were used in the GPS analysis. Thick lines between GPS stations show the subnet used for the peak ground displacement (PGD) analysis (Fig. 3). White squares, broadband seismometers; light-filled squares, strong-motion instruments; dark-filled squares, co-located broadband and strong-motion instruments. Anchorage is covered in strong-motion instruments at the northeastern end of Cook Inlet. Several clusters on the west side of Cook Inlet indicate locations of volcanoes. Note that a few GPS and seismic stations are co-located (GPS is plotted on top of seismic marker), but most of the GPS stations are at a significant distance from the nearest seismic station. Thin irregular lines in the background indicate faults. Large circles around the epicenter show the *P*-wavefront as the *S* wave reaches the surface at the epicenter for a hypocentral depth of 130, 50, and 12 km (from large to small radius). (Inset) Enlarged view of Augustine Volcano. The color version of this figure is available only in the electronic edition.

several hundred kilometers of the earthquake were saturated or "clipped" for all but the initial *P* wave.

The Alaska Earthquake Center (AEC) generates a series of automated magnitude estimates rapidly after an earthquake. Fifty-two seconds after the Iniskin earthquake, the AEC's first magnitude estimate was M_L 5.9. Although a significant underestimate, this result is due to the clipped data and included only 12 stations, including 7 on Augustine Volcano (Fig. 1). In total, AEC computed 20 solutions in the first 5 min after the earthquake. At 139 s after the OT, the magnitude stabilized to M_L 7.3, based on data from 105 stations. More comprehensive coverage with strong-motion instrumentation would have allowed this magnitude to converge more quickly.

Geodetic Network and Processing

The rupture lies beneath part of the Plate Boundary Observatory (PBO) GPS network, which records continuously at 1 Hz. Four stations in the Anchorage area record at 5 Hz.

Though none of these stations telemeter in real time, UNAVCO, which hosts the National Science Foundation-sponsored PBO facility, responded to the event by downloading 7 days of 1 Hz data before and after the earthquake for stations within a 400-km radius of the epicenter (see Data and Resources). We also use 1 Hz data from two stations operated by the University of Alaska Fairbanks, HDPW and PBAY. The 5 Hz data are available for 12 hrs before and after the event.

The maximum coseismic offsets observed within this network are below 2 cm (Grapenthin and Freymueller, 2016). Given such small permanent displacements induced by the earthquake, determining these in real time to infer the event magnitude from a finite-fault-slip model (e.g., Grapenthin *et al.*, 2014a,b) would be very difficult due to a real-time data variance of about 1 cm or more, depending on the processing strategy (e.g., Grapenthin *et al.*, 2014a; Crowell *et al.*, 2016). Therefore, we neglect the static offsets and focus on the dynamic displacements induced primarily by the *S* waves. We choose a processing strategy that reflects this by following an approach used in northern California (Grapenthin *et al.*, 2014a,b). We process the data as a network of baselines (base-station–rover pairs) using track, which is part of GAMIT/GLOBK developed at the Massachusetts Institute of Technology (MIT; Herring *et al.*, 2010) for postprocessing of subdaily GPS data (i.e., not real time, for which trackRT can be used).

Positions of the rover with respect to the base station are resolved at 1-s intervals using International GNSS Service (IGS) final orbit products (Dow *et al.*, 2009). We use the global pressure and temperature model (Boehm *et al.*, 2006) and the global mapping function (Boehm *et al.*, 2007) to model the atmosphere. Station metadata, such as antenna and receiver information, are extracted from the Receiver Independent Exchange (RINEX) format headers, which allows application of IGS08 antenna-phase-center models (Dow *et al.*, 2009). Position coordinates are produced in local north-east-up (NEU) coordinates at the rover station.

To implement a trigger mechanism, we use short-term average/long-term average (STA/LTA) ratios (Allen, 1978; Ohta *et al.*, 2012). We parameterize the window sizes to 3 and 150 s for short term and long term, respectively. The threshold to determine a pick is set to six STA/LTA standard deviations, based on this particular set of data. Significant testing would be needed to tune this for operational use.
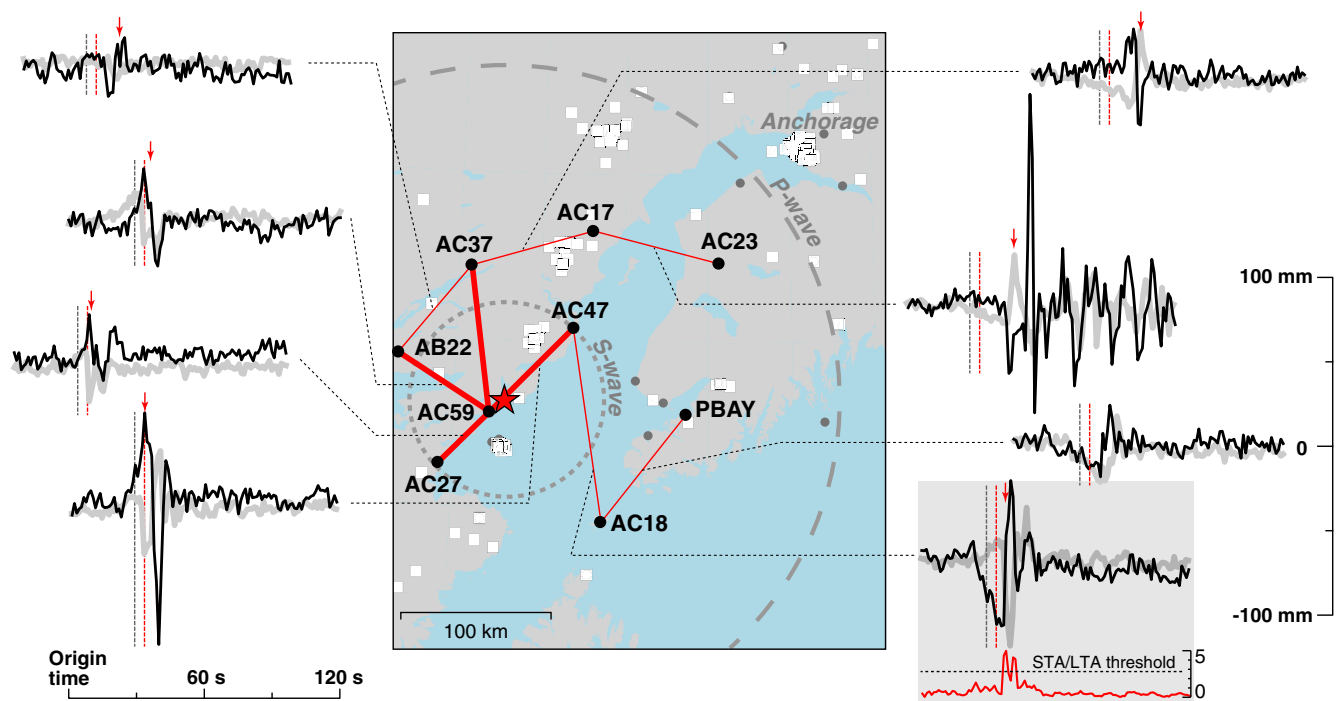
Figure 2. Global Navigation Satellite Systems (GNSS) baselines and corresponding waveforms for rover–base pairs. Each exhibits a clear *S*-wave arrival. Traces are 2-min long, beginning at the origin time, with black and gray representing the north and east components, respectively. All traces are on the same vertical scale, shown at right. The *S* wave takes ~29 s to reach the surface at the epicenter (time marked with first gray vertical bar in each time series). At 32 s after the origin time, four of the baselines (bold lines in map) have exceeded the short-term average/long-term average (STA/LTA) threshold (time marked with second vertical bar in each time series). Arrows above each time series indicate STA/LTA picks. The approximate *S*- and *P*-wavefronts at this time are shown in dashed gray lines. Rover–base pairs are AB22–AC59, AB22–AC37, AC17–AC37, AC17–AC23, AC27–AC59, AC47–AC59, AC18–PBAY, and AC18–AC47. The gray box contains the AC18–AC47 position time series with the respective STA/LTA time series below. The horizontal dashed line indicates the STA/LTA threshold. It is overcome twice, indicating the arrivals at AC18 and AC47, respectively. The color version of this figure is available only in the electronic edition.

Peak ground displacements (PGDs) recorded by GPS are a sum of static and dynamic displacements, such as *S* waves. Crowell *et al.* (2013) used a scaling relationship that is usually applied to seismic data to map ground motion and hypocentral distance *R* to magnitude M_w:

$$\log(\text{PGD}) = A + B\,M_w + C\,M_w \log(R), \qquad (1)$$

in which *A*, *B*, and *C* are coefficients determined in a regression analysis, and PGD is the maximum of the square root of the sum of squares of the north, east, and up displacements (Melgar *et al.*, 2015). They determined values for the scaling parameters that best fit ground displacements from a few recent earthquakes, ranging in magnitude between 5 and 9.0. Melgar *et al.* (2015) updated these parameters as more earthquakes have been recorded by high-rate GPS, and we use their parameter values $A = -4.434 \pm 0.141$, $B = 1.047 \pm 0.022$, and $C = -0.138 \pm 0.003$ to infer the magnitude evolution of the Iniskin earthquake.

Because the PGD analysis requires hypocentral distance (equation 1), we adjust the base–rover displacements, such that each station moves relative to AC51 (Fig. 1), a site that experienced insignificant dynamic motion during the time

interval we examine (100 s from OT). To limit the impact of far-field noise, we reduce the number of stations for the PGD analysis to those encompassed by the network shown in bold lines in Figure 1.

Results

Sample time series in the east and north components over the first 2 min after the event OT are presented in Figure 2. Although the time series represent a diverse geographic station distribution, it is difficult to make out any substantial permanent coseismic offsets, which is not surprising given the depth of the earthquake. More striking, however, is how well the azimuthal variations in ground motion are resolved. These are the combined influence of the radiation pattern, rupture directivity, and variations in ground response. The individual contributions of these factors are difficult to distinguish from the existing data set.

The most significant dynamic motion is recorded at stations AC17, AC23, and AC47 within the Cook Inlet basin (Fig. 2). Of these, AC23, on the Kenai Peninsula, experiences the largest ground motion with a displacement maximum of 10 cm in the north component. Strong basin reverberations are recorded at AC23 for more than 3 min.
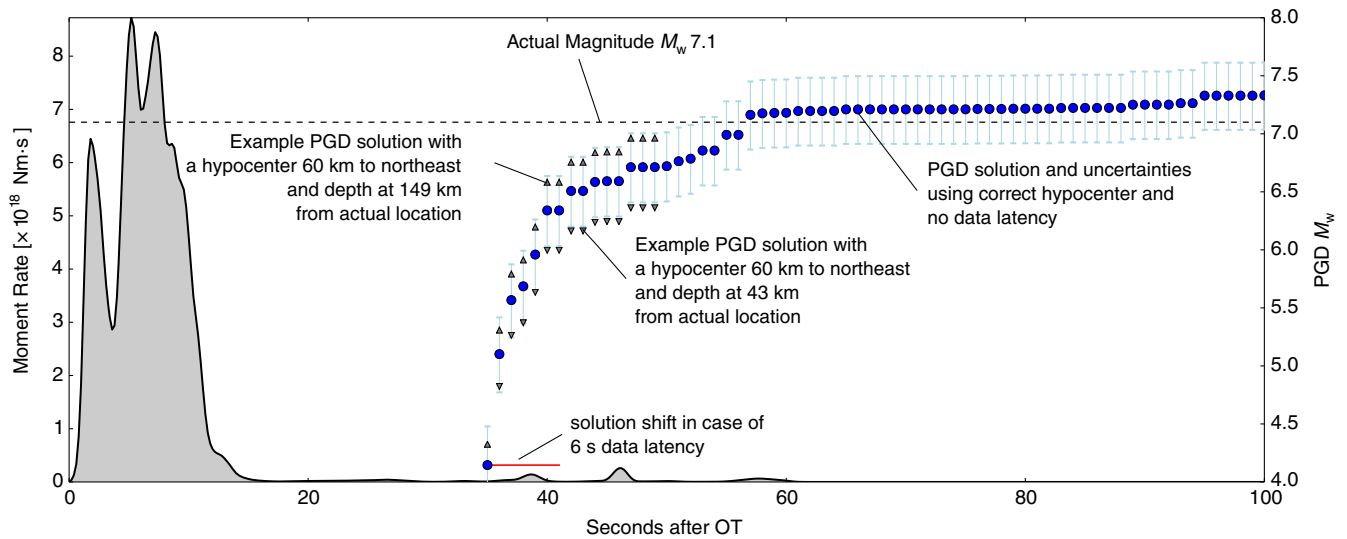
Figure 3. PGD magnitude estimates (filled circles) and uncertainties and U.S. Geological Survey (USGS) moment-rate function (solid line) with respect to the origin time. Solutions based on mislocated hypocenters (gray triangles) are labeled; the solid horizontal bar attached to the first magnitude solution indicates temporal shift of the solution due to, for instance, 6 s of data latency. The dotted line indicates the actual magnitude. First magnitude estimates are available after 35 s. We estimate at 40 s $M_w \sim 6.0$, at 47 s $M_w \sim 6.7$, and at 55 s $M_w \sim 7.0$. The color version of this figure is available only in the electronic edition.

Baselines AC27–AC59 and AB22–AC59 to the south and west of the epicenter exhibit dynamic motion recorded at AC59 but no secondary arrivals at AB22 or AC27. This is typical for most other stations to the south, indicating smaller ground-motion intensities. For baseline AC47–AC59, to the northeast of the epicenter, however, the dynamic motion recorded at AC59 is quickly overwhelmed by a much stronger *S*-wave arrival at AC47.

To the east of the epicenter, AC18–PBAY records only slight dynamic deformation at PBAY, too small to exceed the STA/LTA threshold. AC18–AC47, on the other hand, moves significantly, due to the motion at AC47 described above.

A sample STA/LTA evolution and pick for *S*-wave arrival at 36 s past OT is given for AC18–AC47 in Figure 2. The earliest picks are at 32 s after OT when the *S* wave passes AC59 or about 3 s after the *S* wave arrives at the surface from 125 km depth. Displacements usually begin 1–2 s before the STA/LTA pick because overcoming our high threshold consumes additional time.

The surface locations of *P*-wave and *S*-wavefronts 32 s after OT are visualized in Figure 2 with STA/LTA-triggered rover–base station pairs marked in bold. Although the *P* wave has not yet arrived in Anchorage, which happens about 36 s after OT, it has traversed a significant number of seismic stations in the area (Fig. 2, white squares). In an EEW scenario, many of these would be contributing to trigger algorithms (e.g., Kuyuk *et al.*, 2014), though as discussed above, most of these broadbands would be expected to saturate. For earthquakes at shallower depths, however, the difference between the radii of the *P* and *S* waves would be smaller. In such a scenario, four GNSS *S*-wave triggers could be achieved before the *P* wave had traversed as many seismic

stations. Notably, the *S* wave has not yet arrived on the Kenai Peninsula, and the marked GNSS triggers (Fig. 2) could contribute to a >2 s warning for the communities on the southern tip of the peninsula.

The results from the PGD magnitude analysis are presented in Figure 3 (filled circles). This solution is based on the final hypocenter location and assumes no data latency. The impact of significantly mislocated hypocenters is shown with gray triangles for the first 10–15 s of solutions, after which we assume convergence to the final location. These magnitudes fall mostly within the uncertainties of the final location solution, because only the base-10 logarithm of hypocentral distances enters equation (1). A fairly large latency of 6 s, similar to the latency during the 2014 Napa earthquake (Grapenthin *et al.*, 2014a) and the median of the simulations by Crowell *et al.* (2016), would introduce a shift of the solution to the right along the time axis, as indicated by the solid horizontal bar attached to the first solution in Figure 3.

The first magnitude estimate of M_w 4.1 is available at 35 s after OT. Within 5 s this increases to M_w 6.4. It takes another 7 s to reach M_w 6.7. At 57 s after OT, the PGD-derived magnitude had reached M_w 7.2. This is just 41 s after the *P* wave first reached the surface at the epicenter. The potential to contribute an accurate magnitude in less than 1 min, for an M_w 7+ earthquake at depth, is a clear demonstration of the value of GNSS-based magnitudes.

Discussion

An operational system that incorporates GNSS *S*-wave detections must tweak the STA/LTA parameters to avoid triggering on surface waves, teleseisms, and other signals that increase the signal-to-noise ratio. This is quite similar to
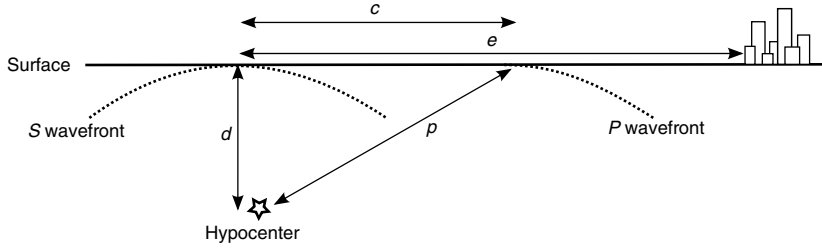
Figure 4. Schematic of the depth–wavefront geometry and the importance of epicentral distance e relative to earthquake depth d for meaningful GNSS-based warning. Once the S wave has traveled distance d to the surface, the P wave will have traveled distance $p = \frac{d}{V_S} \times V_P$, which relates to an epicentral distance at the surface $c = \sqrt{p^2 - d^2}$. As long as e is greater than c plus some network density adjustment, GNSS could potentially contribute to the earthquake early warning (EEW) trigger algorithm (equation 2). Otherwise, the P wave may already be detected within a dense local seismic network, such as is installed in Anchorage (Fig. 1).

the work required for P-wave detections (e.g., Kuyuk *et al.*, 2014). Additionally, more sophisticated phase-picking algorithms, such as Wavelet-based approaches (e.g., Rinehart *et al.*, 2016), might result in lower false-positive rates, compared with the traditional approach employed here.

Although we use final orbits and postprocessed positioning solutions, results using real-time orbit products would be only slightly noisier at the frequencies of interest. Crowell *et al.* (2016) showed that, for a similarly sized earthquake, realistic noise, latency, and dropouts result in magnitude estimates within about 0.3 magnitude units of the target magnitude and realistic depth estimates.

The determination of the PGD magnitude requires the hypocentral distance between earthquake and observing station and hence a depth estimate for the event. Earthquake depths are difficult to determine, even in non-real-time environments. EEW systems operating in regions with only shallow crustal faults can reduce the complexity by assuming a fixed depth during location searches (e.g., Böse *et al.*, 2014). This will result in biased magnitudes derived with the PGD approach. To circumvent this issue, Crowell *et al.* (2016) implement a 1-km depth grid search in G-FAST, over which they estimate the PGD magnitude and determine the best result, based on a maximum variance reduction. This search could be initiated by GNSS S-wave detections alone.

The low initial magnitude estimate reflects the reality that it took 10–15 s for the source processes of this earthquake to complete. This is a significant complication for the concept of early warning. For a larger earthquake, such as the 1964 M_w 9.2 Great Alaska earthquake, which ruptured the subduction megathrust up-dip of the Iniskin earthquake, attempts to derive a magnitude within the first 4 min would inherently produce an underestimate. The evolving PGD magnitude of the Iniskin earthquake, with a final estimate of 22 s after the first detection (Fig. 3), offers a small glimpse at this problem. Adding the source duration and the travel time to the surface suggests that an accurate P-wave magnitude would not be theoretically possible until 25–30 s after

the OT. For an S-wave-derived magnitude, this theoretical limit would be about 45 s. Directionality of energy release toward Cook Inlet may impact the PGD estimate too. We suggest that most of the nearby stations are not in the direction toward which most of the energy travels (Figs. 1 and 2), although the Cook Inlet basin effect also needs to be untangled from the differences in site responses shown in Figure 2. It takes stations on the Kenai Peninsula, which begin to contribute significantly about 50 s after OT, to increase the PGD magnitude toward its actual size. Without these real-world effects, the final magnitude could have been available several seconds earlier. Regardless, the GNSS data demonstrate an ability to contribute accurate magnitudes more quickly than what actually occurred and is on par with potential seismic-only techniques.

The Iniskin earthquake is a less-than-optimal scenario for the inclusion of S waves into EEW warnings (Fig. 2). Assuming P- and S-wave velocities of 8 and 4.5 km/s, respectively, the P wave reaches the surface 16 s after the OT, at which point the S wave is still 58 km underground. At this velocity, it takes the P wave about 36 s to reach the surface in Anchorage, which is 9 s after the S waves reach the surface at the epicenter. However, an event at similar depth located further west or at shallower depth in the same location would yield a potentially significant impact of GNSS triggers. The 2015 M_w 7.8 Gorkha earthquake in Nepal (Galetzka *et al.*, 2015) is an example of a shallow event within a sparse seismic network. Two existing GNSS sites (KKN4 and CHLM) could possibly have contributed to an early warning shortly before the S wave reached Kathmandu.

It is clear that the depth d of an earthquake and its epicentral distance e from an asset (e.g., a city) help determine whether or not S-wave detections can contribute meaningfully in generating an early warning. We derive a simple relationship (equation 2, Fig. 4) to identify cases for which GNSS might contribute to an early warning:

$$e_t = \sqrt{\left(\frac{d}{V_S} \times V_P\right)^2 - d^2} + n \times i, \qquad (2)$$

in which V_S and V_P are S- and P-wave velocities, respectively; i is the average interstation distance; n represents the number of required GNSS station triggers (in addition to seismic triggers); and e_t is the threshold distance, for which assets with epicentral distance $e > e_t$ can benefit from GNSS triggers. The second term, $n \times i$, is a proxy for network density, whereas the first term represents an absolute minimum distance based on the wave propagation speeds.

Applying equation (2) to the Iniskin earthquake and setting V_S and V_P to 4.5 and 8 km/s as before, we find that $e_t =$

191 km for $d = 130$ km, if we neglect the station density. Because there are several strong-motion stations closer than 191 km, it is unclear how valuable GNSS-derived S-wave observations would have been in this particular case. The situation would be quite different though if the depth was only 50 km ($e_t = 74$ km) or 12 km ($e_t = 18$ km) (see large circles in Fig. 1), which could result from events on the megathrust (the epicenter would be further to the southeast but could be at the same epicentral distance from Anchorage) or from a rupture of one of the major crustal faults in the Cook Inlet region (e.g., Haeussler *et al.*, 2000).

Conclusions

S wave triggers from GNSS receivers are currently not utilized in EEW systems. Our postevent analysis of the 2016 M_w 7.1 Iniskin earthquake in Cook Inlet, Alaska, demonstrates the utility of such triggers, particularly for shallow earthquakes in regions within sparse seismic networks. Adding GNSS S-wave triggers to the early warning detection is straightforward. Combined analysis with the seismic triggers could, in some cases, result in faster alerts and, in most cases, in rapid confirmation or rejection of a warning that was issued based on seismic analysis alone. This earthquake illustrates the different challenges, as well as potential strengths, of early warning systems in subduction zones, compared with systems designed for urban shallow-fault systems.

Although the high-rate GPS time series for the Iniskin earthquake cannot resolve significant permanent displacements, they exhibit significant spatial variations in dynamic motion, mostly due to the impact of the Cook Inlet basin but likely also impacted by radiation pattern and directionality effects. The PGD magnitude analysis shows that GNSS S waves are sufficient to derive a realistic magnitude for the Iniskin earthquake faster than the current seismic-based magnitude tools and, in this case, before strong shaking reached Anchorage.

We derive a simple relationship that indicates whether S-wave triggers would contribute to an early warning by relating earthquake depth to distance of assets receiving early warning. Given the differences in P- and S-wave velocities, GNSS is most helpful for shallow earthquakes. However, we expect that even in subduction zone areas with hypocenters in the 50 km range, GNSS-based S-wave triggers can expedite warning times or make warnings more robust.

Data and Resources

All the original Global Positioning System (GPS) data in Receiver Independent Exchange Format (RINEX) format are available from UNAVCO. For details on data access see https://www.unavco.org/highlights/2016/iliamna.html (last accessed August 2016). Details on the U.S. Geological Survey (USGS) finite-fault model are available at http://earthquake.usgs.gov/earthquakes/eventpage/us10004gqp#finite-fault (last accessed August 2016). Information on damage and ground motion is available via the Alaska Earthquake Center at http://earthquake.alaska.edu/event/12496371 and http://earthquake.alaska.edu/m71-iniskin-earthquake-evolving-content (last accessed August 2016). Figures were made with Generic Mapping Tool (GMT; Wessel and Smith, 1998) and Matplotlib (Hunter, 2007).

References

Allen, R. M., and H. Kanamori (2003). The potential for earthquake early warning in southern California, *Science* **300,** 786–789, doi: 10.1126/science.1080912.

Allen, R. V. (1978). Automatic earthquake recognition and timing from single traces, *Bull. Seismol. Soc. Am.* **68,** 1521–1532.

Boehm, J., R. Heinkelmann, and H. Schuh (2007). Short note: A global model of pressure and temperature for geodetic applications, *J. Geodes.* **81,** 679–683, doi: 10.1007/s00190-007-0135-3.

Boehm, J., A. Niell, P. Tregoning, and H. Schuh (2006). Global mapping function (GMF): A new empirical mapping function based on numerical weather model data, *Geophys. Res. Lett.* **33,** L07304, doi: 10.1029/2005GL025546.

Böse, M., R. Allen, H. Brown, G. Gua, M. Fischer, E. Hauksson, T. Heaten, M. Hellweg, M. Liukis, D. Neuhauser, *et al.* (2014). Early warning for geological disasters, in *Early Warning for Geological Disasters, Advanced Technologies in Earth Sciences*, F. Wenzel and J. Zschau (Editors), Springer, Berlin, Heidelberg, 49–69, doi: 10.1007/978-3-642-12233-0.

Brocher, T. M., A. S. Baltay, J. L. Hardebeck, F. F. Pollitz, J. R. Murray, A. L. Llenos, D. P. Schwartz, J. L. Blair, D. J. Ponti, J. J. Lienkaemper, *et al.* (2015). The M_w 6.0 24 August 2014 South Napa earthquake, *Seismol. Res. Lett.* **86,** 309–326, doi: 10.1785/0220150004.

Colombelli, S., R. M. Allen, and A. Zollo (2013). Application of real-time GPS to earthquake early warning in subduction and strike-slip environments, *J. Geophys. Res.* **118,** 3448–3461, doi: 10.1002/jgrb.50242.

Crowell, B. W., D. Melgar, Y. Bock, J. S. Haase, and J. Geng (2013). Earthquake magnitude scaling using seismogeodetic data, *Geophys. Res. Lett.* **40,** 6089–6094, doi: 10.1002/2013GL058391.

Crowell, B. W., D. A. Schmidt, P. Bodin, J. E. Vidale, J. Gomberg, J. R. Hartog, V. C. Kress, T. I. Melbourne, M. Santillan, S. E. Minson, *et al.* (2016). Demonstration of the Cascadia G-FAST geodetic earthquake early warning system for the Nisqually, Washington, earthquake *Seismol. Res. Lett.* **87,** no. 4, doi: 10.1785/0220150255.

Dow, J. M., R. E. Neilan, and C. Rizos (2009). The International GNSS Service in a changing landscape of Global Navigation Satellite Systems, *J. Geodes.* **83,** 191–198, doi: 10.1007/s00190-008-0300-3.

Fang, R., C. Shi, W. Song, G. Wang, and J. Liu (2014). Determination of earthquake magnitude using GPS displacement waveforms from real-time precise point positioning, *Geophys. J. Int.* **196,** 461–472, doi: 10.1093/gji/ggt378.

Galetzka, J., D. Melgar, J. F. Genrich, J. Geng, S. Owen, E. O. Lindsey, X. Xu, Y. Bock, J.-P. Avouac, L. B. Adhikari, *et al.* (2015). Slip pulse and resonance of the Kathmandu basin during the 2015 Gorkha earthquake, Nepal, *Science* **349,** 1091–1095, doi: 10.1126/science.aac6383.

Given, D. D., E. S. Cochran, T. H. Heaton, E. Hauksson, R. M. Allen, M. Hellweg, J. Vidale, and P. Bodin (2014). Technical implementation plan for the ShakeAlert production system: An earthquake early warning system for the West Coast of the United States, *U.S. Geol. Surv. Open-File Rept. 2014-1097*, 25 pp., doi: 10.3133/ofr20141097.

Grapenthin, R., and J. T. Freymueller (2016). The 2016 M_w 7.1 Iniskin, Alaska, earthquake as seen by high-rate GPS and early warning potential, presented at the *Annual Meeting of the SSA*, Reno, Nevada, 20–22 April 2016.

Grapenthin, R., I. A. Johanson, and R. M. Allen (2014a). The 2014 M_w 6.0 Napa earthquake, California: Observations from real-time GPS-enhanced earthquake early warning, *Geophys. Res. Lett.* **41,** 8269–8276, doi: 10.1002/2014GL061923.

Grapenthin, R., I. A. Johanson, and R. M. Allen (2014b). Operational real-time GPS-enhanced earthquake early warning, *J. Geophys. Res.* **119,** 7944–7965, doi: 10.1002/2014JB011400.

Gutenberg, B. (1945). Amplitudes of surface waves and magnitudes of shallow earthquakes, *Bull. Seismol. Soc. Am.* **35,** 3–12.

Haeussler, P. J., R. L. Bruhn, and T. L. Pratt (2000). Potential seismic hazards and tectonics of the upper Cook Inlet basin, Alaska, based on analysis of Pliocene and younger deformation, *Bull. Geol. Soc. Am.* **112,** 1414–1429, doi: 10.1130/0016-7606(2000)112<1414:PSHATO>2.0.CO;2.

Herring, T. A., R. W. King, and S. C. McClusky (2010). *GAMIT/GLOBK Reference Manuals, Release 10.4*, available at http://www-gpsg.mit.edu/~simon/gtgk/GLOBK_Ref.pdf and http://www-gpsg.mit.edu/~simon/gtgk/GAMIT_Ref.pdf (last accessed August 2016).

Hoshiba, M., K. Iwakiri, N. Hayashimoto, and T. Shimoyama (2011). Outline of the 2011 off the Pacific coast of Tohoku earthquake (M_w 9.0)—Earthquake early warning and observed seismic intensity—, *Earth Planets Space* **63,** no. 7, 547–551, doi: 10.5047/eps.2011.05.031.

Hunter, J. D. (2007). Matplotlib: A 2D graphics environment, *Comput. Sci. Eng.* **9,** 90–95.

Kawamoto, S., Y. Hiyama, Y. Ohta, and T. Nishimura (2016). First result from the GEONET real-time analysis system (REGARD): The case of the 2016 Kumamoto earthquakes, *Earth Planets Space* **68,** doi: 10.1186/s40623-016-0564-4.

Kuyuk, H. S., R. M. Allen, H. Brown, M. Hellweg, I. Henson, and D. Neuhauser (2014). Designing a network-based earthquake early warning algorithm for California: ElarmS-2, *Bull. Seismol. Soc. Am.* **104,** 162–173, doi: 10.1785/0120130146.

Melgar, D., B. W. Crowell, Y. Bock, and J. S. Haase (2013). Rapid modeling of the 2011 M_w 9.0 Tohoku-oki earthquake with seismogeodesy, *Geophys. Res. Lett.* **40,** 2963–2968, doi: 10.1002/grl.50590.

Melgar, D., B. W. Crowell, J. Geng, R. M. Allen, Y. Bock, S. Riquelme, E. M. Hill, M. Protti, and A. Ganas (2015). Earthquake magnitude calculation without saturation from the scaling of peak ground displacement, *Geophys. Res. Lett.* **42,** 5197–5205, doi: 10.1002/2015GL064278.

Minson, S. E., J. R. Murray, J. O. Langbein, and J. S. Gomberg (2014). Real-time inversions for finite fault slip models and rupture geometry based on high-rate GPS data, *J. Geophys. Res.* **119,** 3201–3231, doi: 10.1002/2013JB010622.

Ohta, Y., T. Kobayashi, H. Tsushima, S. Miura, R. Hino, T. Takasu, H. Fujimoto, T. Iinuma, K. Tachibana, T. Demachi, *et al.* (2012). Quasi real-time fault model estimation for near-field tsunami forecasting based on RTK-GPS analysis: Application to the 2011 Tohoku-Oki earthquake (M_w 9.0), *J. Geophys. Res.* **117,** no. B02311, doi: 10.1029/2011JB008750.

Rinehart, A. J., S. A. Mckenna, and S. T. Dewers (2016). Using wavelet covariance models for simultaneous picking of overlapping *P*- and *S*-wave arrival times in noisy single-component data, *Seismol. Res. Lett.* **87,** no. 4, doi: 10.1785/0220150130.

Simons, M., S. E. Minson, A. Sladen, F. Ortega, J. Jiang, S. E. Owen, L. Meng, J.-P. Ampuero, S. Wei, R. Chu, *et al.* (2011). The 2011 magnitude 9.0 Tohoku-Oki earthquake: Mosaicking the megathrust from seconds to centuries, *Science* **332,** 1421–1425, doi: 10.1126/science.1206731.

Wessel, P., and W. H. F. Smith (1998). New, improved version of generic mapping tools released, *Eos Trans. AGU* **79,** 579–579, doi: 10.1029/98EO00426.

Worden, C. B., M. C. Gerstenberger, D. A. Rhoades, and D. J. Wald (2012). Probabilistic relationships between ground-motion parameters and modified Mercalli intensity in California, *Bull. Seismol. Soc. Am.* **102,** 204–221, doi: 10.1785/0120110156.

Wright, T. J., N. Houlié, M. Hildyard, and T. Iwabuchi (2012). Real-time, reliable magnitudes for large earthquakes from 1 Hz GPS precise point positioning: The 2011 Tohoku-Oki (Japan) earthquake, *Geophys. Res. Lett.* **39,** no. 12, doi: 10.1029/2012GL051894.

Department of Earth and Environmental Science
New Mexico Institute of Mining and Technology
801 Leroy Place, MSEC 356
Socorro, New Mexico 87801
rg@nmt.edu
   (R.G.)

Alaska Earthquake Center
University of Alaska Fairbanks
Fairbanks, Alaska 99775
   (M.W.)

Geophysical Institute
University of Alaska Fairbanks
903 Koyukuk Drive
Fairbanks, Alaska 99775-7320
   (J.F.)